

The variability of accretion onto Schwarzschild black holes from turbulent magnetized discs

Philip J. Armitage^{1,2*} and Christopher S. Reynolds^{3†}

¹*JILA, University of Colorado, 440 UCB, Boulder CO 80309-0440, USA*

²*Department of Astrophysical and Planetary Sciences, University of Colorado, Boulder CO 80309-0391, USA*

³*Department of Astronomy, University of Maryland, College Park MD 20742, USA*

arXiv:astro-ph/0302271v1 13 Feb 2003

30 October 2018

ABSTRACT

We use global magnetohydrodynamic simulations, in a pseudo-Newtonian potential, to investigate the temporal variability of accretion discs around Schwarzschild black holes. We use the vertically-averaged magnetic stress in the simulated disc as a proxy for the rest-frame dissipation, and compute the observed emission by folding this through the transfer function describing the relativistic beaming, light bending and time delays near a non-rotating black hole. The temporal power spectrum of the predicted emission from individual annuli in the disc is described by a broken power law, with indices of ≈ -3.5 at high frequency and ≈ 0 to -1 at low frequency. Integrated over the disc, the power spectrum is approximated by a single power law with an index of -2 . Increasing inclination boosts the relative power at frequencies around $\approx 0.3f_{\text{ms}}$, where f_{ms} is the orbital frequency at the marginally stable orbit, but no evidence is found for sharp quasi-periodic oscillations in the lightcurve. Assuming that fluorescent iron line emission locally tracks the continuum flux, we compute simulated broad iron line profiles. We find that relativistic beaming of the non-axisymmetric emission profile, induced by turbulence, produces high-amplitude variability in the iron line profile. We show that this substructure within the broad iron line profile can survive averaging over a number of orbital periods, and discuss the origin of the anomalous X-ray spectral features, recently reported by Turner et al. (2002) for the Seyfert galaxy NGC 3516, in the context of turbulent disc models.

Key words: accretion, accretion discs — black hole physics — MHD — turbulence — X-rays: binaries — galaxies: active

1 INTRODUCTION

A major aim of the astrophysical study of black holes is to determine the fundamental parameters of a rotating black hole – the mass M and spin parameter a – from astronomical observations. For Galactic black hole candidates such as Cygnus X-1, GRO J1655-40 and GRS 1915+105, the temporal power spectrum holds promise as a route to achieving this goal (van der Klis 2000). The variability of these sources is conventionally described as the superposition of a broadband noise component with one or more quasi-periodic oscillations (QPOs), whose frequencies presumably encode information about the inner accretion flow and black hole properties. For AGN, where the long dynamical times associated with supermassive black holes hamper similar studies,

the main focus is on inferring black hole properties from the profiles of relativistically broadened iron emission lines arising from near the marginally stable orbit (Fabian et al. 1989; Tanaka et al. 1995; Nandra et al. 1997; Wilms et al. 2001; Lee et al. 2002). Iron line profiles themselves are highly variable (Iwasawa et al. 1996).

For accreting black holes, and for other relativistically compact objects, the observed lightcurve arises from the modulation of rest-frame variability (i.e. variability that would be detected by an observer orbiting with the disc gas) by photon propagation effects. Since there is now a consensus that magnetorotational instabilities (MRI, Balbus & Hawley 1991; Balbus & Hawley 1998) provide a source of angular momentum transport in well ionized discs, an unavoidable source of rest-frame variability is the fluctuating dissipation inherent to magnetohydrodynamic (MHD) disc turbulence. Simulations of the MRI show that the high frequency temporal power spectra of the mass accretion

* email: pja@jila1.colorado.edu

† email: chris@astro.umd.edu

rate and magnetic stress display steep power-law spectra (Kawaguchi et al. 2000; Hawley & Krolik 2001, 2002), and suggest that the broadband noise component of observed power density spectra may be identified with the temporal fluctuations of MHD disc turbulence. Spatial fluctuations in the dissipation may also play an important role. For a disc inclined to the line of sight, beaming enhances the emission from the approaching side of the disc relative to that from the receding side. The combination of this photon propagation effect with any source of persistent non-axisymmetric dissipation in the inner regions of the disc could lead to high frequency QPOs in the lightcurve (e.g. Abramowicz et al. 1991; Karas 1999).

In this paper, we use non-relativistic global MHD simulations of the MRI (Armitage 1998; Hawley 2000; Arlt & Rudiger 2001) to model the rest-frame variability of accretion onto a Schwarzschild black hole. A pseudo-Newtonian potential (Paczynski & Wiita 1980) is used to describe the gravitational potential in the vicinity of such a black hole. We extend recent three-dimensional numerical studies of black hole accretion (Hawley 2000; Hawley & Krolik 2001; Armitage, Reynolds & Chiang 2001; Hawley 2001; Reynolds & Armitage 2001; Hawley, Balbus & Stone 2001; Machida, Matsumoto & Mineshige 2001; Hawley & Krolik 2002; Igumenshchev & Narayan 2002; Machida & Matsumoto 2003; Igumenshchev, Narayan & Abramowicz 2003) by taking full account of the distinction between the rest-frame disc emission and that seen by a distant observer. We use these simulations to study both the predicted power spectra from black holes accreting via a geometrically thin disc, and the expected variability of the iron line emission that has been observed in the X-ray spectra of Seyfert galaxies (Tanaka et al. 1995; Wilms et al. 2001; Lee et al. 2002) and Galactic Black Hole Candidates (Balucinska-Church & Church 2000; Miller et al. 2002). The details of the MHD simulations are presented in Section 2, while Section 3 describes our computation of the observed continuum and line emission taking into account relativistic photon propagation. Predicted temporal power spectra are presented in Section 4. In Section 5, we explore our predictions for variability of the broad iron line. It is suggested that the non-axisymmetric structure discussed in this paper may already have been observed in *Chandra* High Energy Transmission Grating (HETG) data for the Seyfert galaxy NGC 3516, and we proceed to quantify the nature of the variability that might be observed in the future, using higher signal-to-noise *Constellation-X* data. Our results, predictions and speculations are summarized in Section 6.

2 THE MHD SIMULATIONS

We model the accretion disc around a non-rotating black hole using ideal, Newtonian MHD. The fluid is assumed to be isothermal, with sound speed c_s , so the equations to be solved are,

$$\frac{\partial \rho}{\partial t} + \nabla \cdot (\rho \mathbf{v}) = 0 \quad (1)$$

$$\frac{\partial \mathbf{S}}{\partial t} + \nabla \cdot (\mathbf{S} \mathbf{v}) = -\nabla P - \rho \nabla \Phi + \mathbf{J} \times \mathbf{B} \quad (2)$$

$$\frac{\partial \mathbf{B}}{\partial t} = \nabla \times (\mathbf{v} \times \mathbf{B}) \quad (3)$$

$$P = \rho c_s^2, \quad (4)$$

where $\mathbf{S} = \rho \mathbf{v}$ is the momentum field and the other symbols have their usual meanings. These equations are solved using the ZEUS MHD code (Stone & Norman 1992a, 1992b), operating in cylindrical polar co-ordinates (z, r, ϕ) . ZEUS is a fixed-grid, time-explicit Eulerian code which uses an artificial viscosity to handle shocks, and a combination of constrained transport (Evans & Hawley 1988) and the method of characteristics (Stone & Norman 1992b) to evolve the magnetic fields. When operated using van Leer advection, as in this work, it is formally of second order accuracy.

A pseudo-Newtonian gravitational potential (Paczynski & Wiita 1980) is used to mimic the effects of general relativity near a non-rotating black hole of mass M ,

$$\Phi = -\frac{GM}{r - r_g}, \quad (5)$$

where $r_g = 2GM/c^2$. This potential reproduces the presence of a marginally stable circular orbit at $r_{\text{ms}} = 6GM/c^2$. For computational reasons, we also omit the vertical component of the gravitational force. This ‘cylindrical disc’ approximation has been used in several previous studies (Hawley, Gammie & Balbus 1995; Armitage 1998; Reynolds & Armitage 2001; Hawley 2001; Steinacker & Papaloizou 2002), and greatly reduces the computational cost of global disc simulations. Of course, it also precludes study of physical effects such as the Parker instability and the development of a disc corona (e.g. Miller & Stone 2000).

To investigate variability caused by the combination of a turbulent disc with relativistic beaming effects, it is necessary to model all 2π of the disc in azimuth. Apart from this (trivial) extension, our numerical setup is the same as that which we have used previously (Armitage, Reynolds & Chiang 2001; Reynolds & Armitage 2001). A hydrodynamically stable disc flow, threaded by a weak vertical magnetic field, is set up as the initial state of the simulations. We begin by defining a Gaussian surface density profile, centred at $4 r_{\text{ms}}$, where r_{ms} is the radius of the marginally stable circular orbit, with a width of $2.66 r_{\text{ms}}$. This disc, initialized with Keplerian angular velocity and zero magnetic fields, is run with the code in 1D mode until a numerical equilibrium is attained. We then add a weak vertical magnetic field (ratio of gas to magnetic pressure $\beta = 10^4$) at all radii where the density exceeds a threshold value (set to be approximately 10 percent of the maximum density), and continue the run in 3D. The boundary conditions are periodic in both z and ϕ , and set to outflow at the radial boundaries. ‘Outflow’ boundary conditions are implemented in ZEUS by setting the values of all physical quantities in boundary zones to be equal to their values in the active zones at the edge of the grid.

Two simulations were run, differing only in the adopted sound speed. One run had a ratio of the sound speed to the Keplerian velocity at r_{ms} of $c_s/v_\phi = 0.061$, while a second run had $c_s/v_\phi = 0.041$ at r_{ms} . We will refer to these as the ‘hot’ and ‘cold’ run respectively, though the actual temperature differences are modest. Both simulations were evolved for a total of 140 orbital periods at r_{ms} , in identical computational domains,

$$-0.7r_g < z < 0.7r_g \quad (6)$$

$$0.7r_{\text{ms}} < r < 8r_{\text{ms}} \quad (7)$$

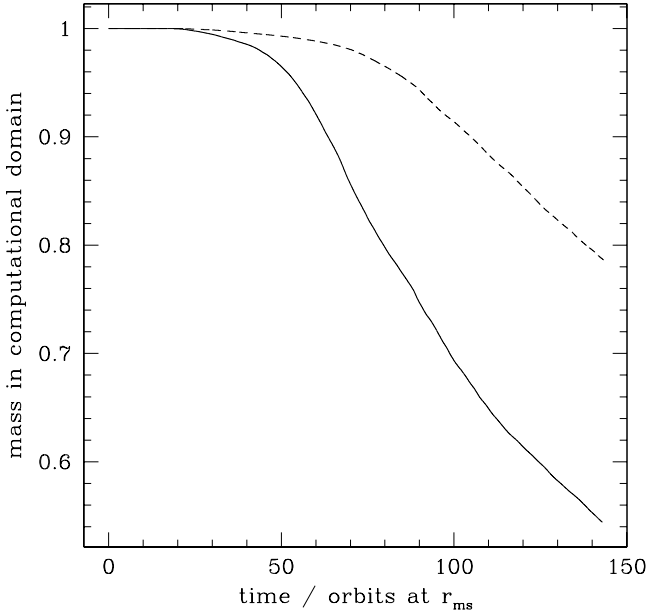


Figure 1. The disc mass as a function of time for the ‘hot’ (solid curve and ‘cold’ (dashed curve) runs, shown as a fraction of the initial disc mass. Only the fully turbulent portion of the run with $t > 50$, where t is measured in units of the orbital period at r_{ms} , is used for analysis of the variability.

$$0 < \phi < 2\pi, \quad (8)$$

with 48 grid points in z , 192 grid points in r , and 288 grid points in ϕ . A non-uniform radial grid, with mesh points spaced such that $r_{i+1} = (1 + \delta)r_i$, with δ a constant, is employed, so that $\Delta r/\Delta\phi$ is constant at all radii. The inner radial boundary was placed as close to the marginally stable orbit as possible (to maximise the timestep which is almost always determined by the azimuthal velocity at r_{in}), but far enough within r_{ms} that the flow across the boundary was both supersonic and super-Alfvénic. As has been noted by Igumenshchev et al. (2003), this inner boundary condition becomes inappropriate if large net amounts of magnetic flux are able to be dragged inward by the accretion flow. Here, we make the assumption – justified in part by the results of Lubow, Papaloizou & Pringle (1994) – that extensive field dragging does not occur for thin discs.

2.1 Properties of the simulations

The basic properties of the MHD disc turbulence seen in the simulations are, unsurprisingly, very similar to those reported previously (i.e. although we need a full 2π in azimuth to study variability, smaller azimuthal domains suffice for most other purposes). Here, we summarize a few features that are pertinent to the subsequent analysis.

Figure 1 shows the total mass in the computational domain as a function of time for the hot and cool runs respectively. Significant accretion commences after around 30 orbits of evolution at the marginally stable orbit. For the hot run, the accretion rate is very roughly constant after around 50 orbits of evolution, and it is this portion of the simulation

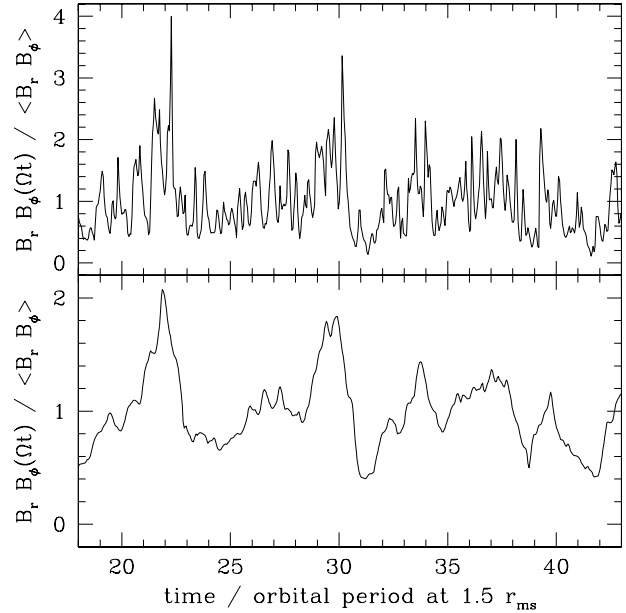


Figure 2. The vertically integrated magnetic stress for the hot disc at a radius of $1.5 r_{\text{ms}}$, evaluated at a single azimuthal point corotating with the local Keplerian angular velocity. The upper panel shows the raw measurement, the lower panel the same curve smoothed over an interval equal to the local orbital period. The stress is shown normalized to the instantaneous average value at the same radius.

which we analyse for variability. Note, however, that there remains a secular trend in the accretion rate even over this latter portion (initially increasing, then decreasing once a significant fraction of the initial mass has been accreted). Since this is an artefact of the computational setup, we can only look at variability on substantially shorter timescales than the run length¹

A single persistent hotspot, orbiting near the innermost stable orbit where relativistic effects are most pronounced, would lead to a strong periodic feature in the lightcurve (Karas 1999). Such QPOs will be diluted in more realistic models, first by the existence of patchy dissipation at *all* radii, and second by the limited lifetime of regions of enhanced dissipation. Figure 2 illustrates the latter point. We plot the magnetic stress, vertically integrated through the disc, at a single point corotating with the local Keplerian orbital velocity. Results for the hot simulation are shown, although very similar results are obtained for the cold case. Large fluctuations are observed, with the peak stress exceeding the local mean by a factor that can be as large as ~ 4 . However, these are also transient features, with a temporal coherence time of only a few orbital periods. If, as we assume later, the magnetic stress provides a proxy for the

¹ Because we have only one realization of each simulation, there are also large *uncertainties* in our estimation of the temporal power spectrum at the lowest frequencies. These purely statistical uncertainties would preclude us from making statements about variability on timescales comparable to the run length, even if the mean accretion rate showed no secular trend.

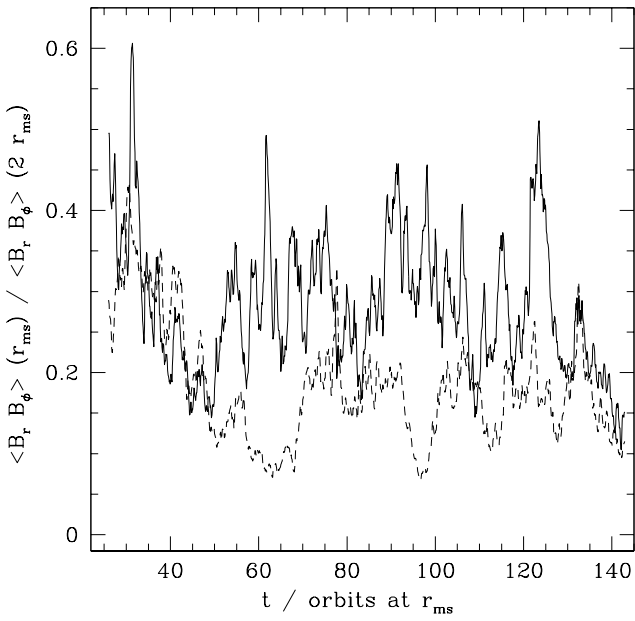


Figure 3. The magnetic torque at the marginally stable orbit as a fraction of the torque in the disc at a radius of $2r_{\text{ms}}$ for the simulations with high (solid line) and low (dashed line) sound speed. Non-zero stress at r_{ms} becomes relatively more important for the disc structure as the disc temperature increases.

disc dissipation, it is clear that ‘hotspots’ arising from MHD disc turbulence will lead to at most broad QPOs in power spectra of the disc emission.

Recent analytic (Krolik 1999; Gammie 1999; Agol & Krolik 2000; Afshordi & Paczynski 2003) and numerical work (Hawley 2000; Armitage, Reynolds & Chiang 2001; Reynolds & Armitage 2001; Hawley & Krolik 2001, 2002) has investigated the possibility that the structure of the inner accretion disc might be modified by the existence of magnetic coupling to gas in the plunging region at $r < r_{\text{ms}}$. The presence of stress at the last stable orbit is potentially important for studies of variability, as a disc with non-zero stress at r_{ms} has a dissipation profile that is more centrally concentrated than a standard disc (Agol & Krolik 2000). Figure 3 shows how important this effect is for our simulations. We plot the mean stress at r_{ms} as a fraction of the stress at $2r_{\text{ms}}$ (this ratio is adopted because the changing accretion rate means that the stress at r_{ms} does not tend to a constant value). At late times, we find that this ratio fluctuates around a value of around 0.3 for the hot disc run. There are, however, large fluctuations, which persist over timescales that can be as long as 10 orbits at r_{ms} . As discussed by Papaloizou & Nelson (2003), and by Winters, Balbus & Hawley (2003), these persistent fluctuations are a generic feature of disc MHD turbulence. They are present in local (e.g. Brandenburg et al. 1995; Winters, Balbus & Hawley 2003) as well as global simulations (Papaloizou & Nelson 2003), and their existence means that averaging over long timescales is needed to recover the mean properties of the flow.

As in previous simulations (Reynolds & Armitage 2001), there is evidence that the contribution of stress at

r_{ms} becomes relatively less important as the sound speed (or, equivalently, the implied disc thickness h/r) is reduced. In our subsequent analysis, we compute both raw lightcurves (which include disc dissipation arising from stress at r_{ms}), and normalized lightcurves which explicitly fix the form of the radial dissipation profile to match the predictions of zero-torque boundary condition disc models. Comparing these lightcurves allows us to investigate whether the presence of stress at the marginally stable orbit has a significant (and potentially observable) effect on the predicted temporal power spectrum.

3 RELATIVISTIC TRANSFER FUNCTION

With a number of approximations, described in Section 4.1, the MHD simulations can be used to define a plausible time-dependent pattern of emission across the disc plane, $F(r, \phi, t)$. When the region of interest is close to the black hole, as it is in this study, one must also account for general relativistic effects (i.e. beaming, light bending and time-delays) in order to determine the appearance of the simulated disc to an observer at infinity. In this section, we briefly discuss how we incorporate these effects.

Suppose the observer is viewing the disc from a large distance at an inclination of i from the normal to the disc plane. We define cartesian coordinates (x, y) on the observer’s image plane such that the origin $x = y = 0$ lies at the center of the event horizon’s image and the y -axis is parallel with the apparent (i.e. projected) normal to the disc. Let us consider a photon that is emitted from the disc at position (r, ϕ) with frequency ν_{em} and is subsequently observed, a Schwarzschild time t later, at position (x, y) on the image plane with frequency ν_{obs} . Our task is to compute the functions $x(r, \phi; i)$, $y(r, \phi; i)$, $t(x, y; i)$, and $g(x, y; i)$, where we have defined the frequency shift factor as

$$g(x, y) = \frac{\nu_{\text{obs}}}{\nu_{\text{em}}}. \quad (9)$$

For a number of inclinations ($i = 1^\circ, 10^\circ, 20^\circ, \dots, 80^\circ$), we integrated null geodesics (photon paths) through the Schwarzschild metric

$$ds^2 = -\left(1 - \frac{2GM}{c^2 r}\right)dt^2 + \left(1 - \frac{2GM}{c^2 r}\right)^{-1}dr^2 + r^2(d\theta^2 + \sin^2\theta d\phi^2), \quad (10)$$

which exactly describes the space-time geometry around a non-rotating and uncharged black hole. Starting from a particular point (x, y) on the image plane, we integrate photon paths down to the disc plane $\theta = \pi/2$ using the first integrals of the geodesic equation (conservation of angular momentum and energy, arising from the ϕ and t independence of the metric, respectively), the Carter constant, and the light-like nature of the path. For these details, we refer the reader to Appendix A of Reynolds et al. (1999). Turning points in the photon orbits are identified and treated using the method of Rauch & Blandford (1994). These integrations allow us to determine the maps $x(r, \phi; i)$, $y(r, \phi; i)$ and $t(x, y; i)$.

The frequency shift factor for a given photon path, g , is given by

$$g = \frac{(p_\mu u^\mu)_{\text{disc}}}{(p_\mu u^\mu)_{\text{obs}}}, \quad (11)$$

where p_μ is the 4-momentum of the photon at the disc/observer, and u^μ is the 4-velocity of the disc/observer. The photon 4-momentum is determined by the photon integration, and we suppose that the observer is stationary (in Schwarzschild coordinates) and very distant from the black hole; thus $u_{\text{obs}}^\mu = (1, 0, 0, 0)$. Hence, we can compute g for any given photon path provided we know the 4-velocity field on the disc plane. Initially, one might be tempted to take the 3-velocity field directly from our MHD simulations (which are approximately ‘Keplerian’ with respect to the modified potential) and construct the appropriate 4-velocity field as input for our computation of g . However, this approach is problematic for the following reason. Since our MHD simulation is intrinsically non-relativistic, and based upon a potential that diverges at the event horizon, the 3-velocities within the simulated plunging region can significantly exceed those that would be found in a relativistic calculation. This would lead to artificially high values of $|g - 1|$, and hence artificially strong relativistic beaming.

Motivated by the fact that the velocity field in our simulated disc is very close to Keplerian with respect to the pseudo-Newtonian potential, we choose instead to use the correct relativistic 4-velocity for test-particle circular motion in our computation of g . This is well defined down to the photon circular orbit at $3GM/c^2$, which lies inside the inner edge of our computational grid. Of course, disc material within some radius close to the radius of marginal stability (at $6GM/c^2$) will no longer be on circular orbits, but the deviations in the relevant parts of the disc are small. Employing this assumption, we compute the function $g(x, y; i)$.

4 TEMPORAL VARIABILITY OF THE SIMULATED FLUX

4.1 The simulated lightcurve

A direct calculation of the emission from the disc would require, first, that we solve an energy equation, and second that we attain sufficient resolution in a global simulation to model a stratified disc and corona (Miller & Stone 2000) where a significant fraction of the dissipation probably occurs. Since our actual calculation is more limited than this, we must instead choose some proxy for the dissipation. Out of several possible proxies, we have opted to follow Hawley & Krolik (2001), and use the magnetic stress as a local tracer of where in the flow dissipation is expected to occur². We then compute lightcurves and power spectra by making the further assumption that the dissipated energy is promptly radiated from the disc.

The most important assumption is obviously the aforementioned one – that *at a given radius, the azimuthal dependence of the emission is proportional to the vertically integrated magnetic stress*. Even given this assumption, however, there is some ambiguity as to the best way to calculate the lightcurve. As described below, we calculate both ‘raw’

² Data storage limitations prompted us to make this basic choice *prior* to running full resolution simulations. During the runs, vertically integrated slices of $B_r B_\phi$ were the only quantities output at high time resolution.

lightcurves, and lightcurves in which the average disc dissipation has been normalized to match an analytic form.

4.1.1 The raw lightcurve

To compute the raw lightcurve, we first calculate the emission map F_{raw} that would be seen by observers orbiting with the disc flow. F_{raw} is given by (e.g. Hubeny & Hubeny 1998).

$$F_{\text{raw}}(r, \phi, t) = \sqrt{\frac{GM}{r^3}} \left(\frac{A}{B} \right) \int B_r B_\phi dz, \quad (12)$$

where the relativistic correction factors are,

$$\begin{aligned} A &= 1 - \frac{2GM}{rc^2} \\ B &= 1 - \frac{3GM}{rc^2}. \end{aligned} \quad (13)$$

Using the transfer function, which gives the mapping between (r, ϕ) in the disc plane and (x, y) in the image plane, we then compute the image that would be seen by a distant observer viewing the disc at a particular inclination angle, i . We assume that the observer images the disc in a fixed spectral band, which introduces a ‘K-correction’ that depends upon the spectrum of the disc emission. If at each radius the energy spectrum is $\propto \nu^{-1}$ (fairly typically for accreting black holes), the resulting image is,

$$I(x, y, t) \propto g^4(x, y) F_{\text{raw}}(r, \phi, t_{\text{emit}}), \quad (14)$$

where one factor of g comes from the K-correction. We allow for the varying flight time of photons from different parts of the accretion disc by distinguishing between the time t_{emit} , at which photons are emitted from the disc, and time t when the photons are observed. Examples of these images are shown in Figure 4. The raw lightcurve at time t_i , $\mathcal{F}(t_i)$ is then simply the sum over the image of the intensity at time t_i at each pixel (x_k, y_k) ,

$$\mathcal{F}(t_i) = \sum_{j, k} I(x_j, y_k, t_i). \quad (15)$$

We emphasize that the predicted variability properties depend upon the assumed emission spectrum from the disc as well as on the statistical fluctuations of MHD disc turbulence. In particular, modeling blackbody emission from the disc would require a different radial weighting of the simulated disc dissipation.

The resulting light curves are shown in Figure 5 for several different inclinations. As already noted, the shape of these lightcurves over the longest timescales reflects only the viscous evolution of the ring of gas used for our initial conditions. There is a secular increase in the inner accretion rate (and accompanying dissipation) as the MRI saturates at increasingly large radii, followed (for the hot simulation) by an eventual decline once a substantial fraction of the gas has been accreted. These slow changes in accretion rate are artefacts of the initial conditions used in the simulation — real accretion discs are long lived objects with very large reservoirs of material. Of more relevance to real systems is the inclination dependence of these light curves. One observes a marked increase in rapid variability for the more edge on systems. This is readily interpreted as the effects of relativistic beaming coupled with the ‘blobby’ nature of

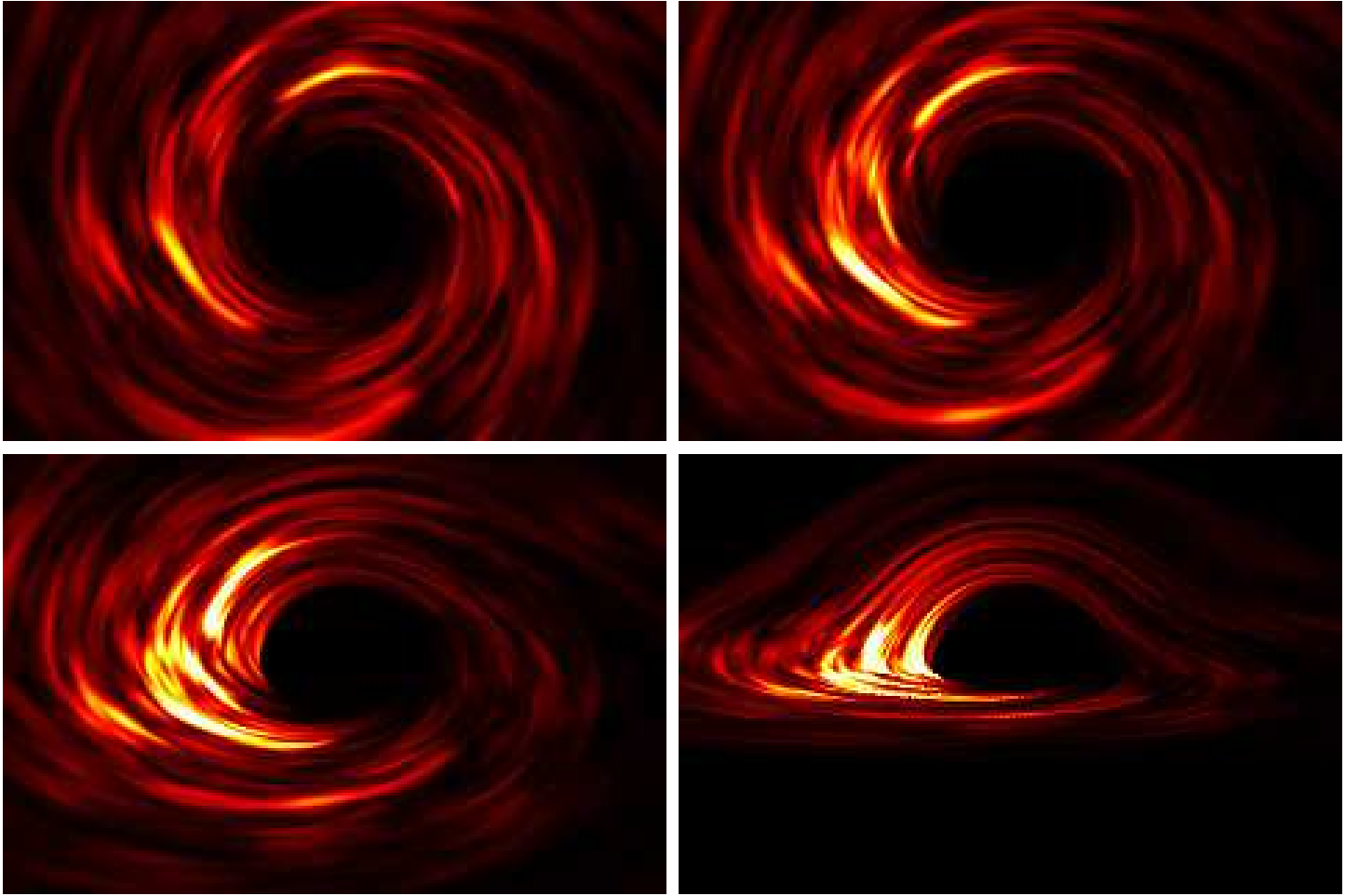


Figure 4. View of the disc as seen by a distant observer at an inclination angle of 5° (upper left), 30° (upper right), 55° (lower left) and 80° (lower right). In these raw images, note the presence of stress extending to the inner boundary of the computational domain, within the marginally stable circular orbit. Movies showing the evolution of the simulated disc are available at http://jilawww.colorado.edu/~pja/black_hole.html.

the simulated emission. We shall explore this point in more detail below when we discuss temporal power spectra.

4.1.2 Novikov-Thorne normalized lightcurve

The raw lightcurve computed from the simulation self-consistently includes the contribution from torque at the marginally stable orbit to the emission of the inner disc. As shown in Figure 3, this contribution can be important, especially for hotter (and therefore geometrically thicker) discs (Reynolds & Armitage 2001). However, because the domain of the simulation is limited, only the inner region of the simulated disc is in a steady-state. The raw lightcurve therefore *underestimates* the contribution to the flux from larger radii in the disc.

Cognisant of this drawback, we also compute lightcurves by combining the simulated fluctuations in the stress (in ϕ and t) with an analytic dissipation profile due to Novikov & Thorne (1973). Specializing to the case of a Schwarzschild black hole, the radial dependence of the disc flux measured by an observer orbiting with the disc gas is (Page & Thorne

1974),

$$F_{\text{NT}}(r) \propto \frac{1}{x^4(x^3 - 3x)} \left[x - \sqrt{6} - \frac{\sqrt{3}}{2} \ln \left(\frac{x - \sqrt{3}}{\sqrt{6} - \sqrt{3}} \right) + \frac{\sqrt{3}}{2} \ln \left(\frac{x + \sqrt{3}}{\sqrt{6} + \sqrt{3}} \right) \right] \quad (16)$$

where,

$$x \equiv \sqrt{\frac{r}{(GM/c^2)}}. \quad (17)$$

Given this dissipation profile, we proceed to construct a lightcurve as before, except that we replace the emission map $F_{\text{raw}}(r, \phi, t)$ with $F_{\text{NT}}(r, \phi, t)$, defined as,

$$F_{\text{NT}}(r, \phi, t) = \frac{B_r B_\phi(r, \phi, t)}{\langle B_r B_\phi \rangle(r)} F_{\text{NT}}(r). \quad (18)$$

In this expression $B_r B_\phi$ in both the numerator and the denominator is understood to be vertically integrated, and the angle brackets denote averaging over both ϕ and t . By construction, the resulting dissipation map $F_{\text{NT}}(r, \phi, t)$ has the same time-averaged dissipation profile as a Novikov-Thorne disc, on top of which are superimposed fluctuations whose

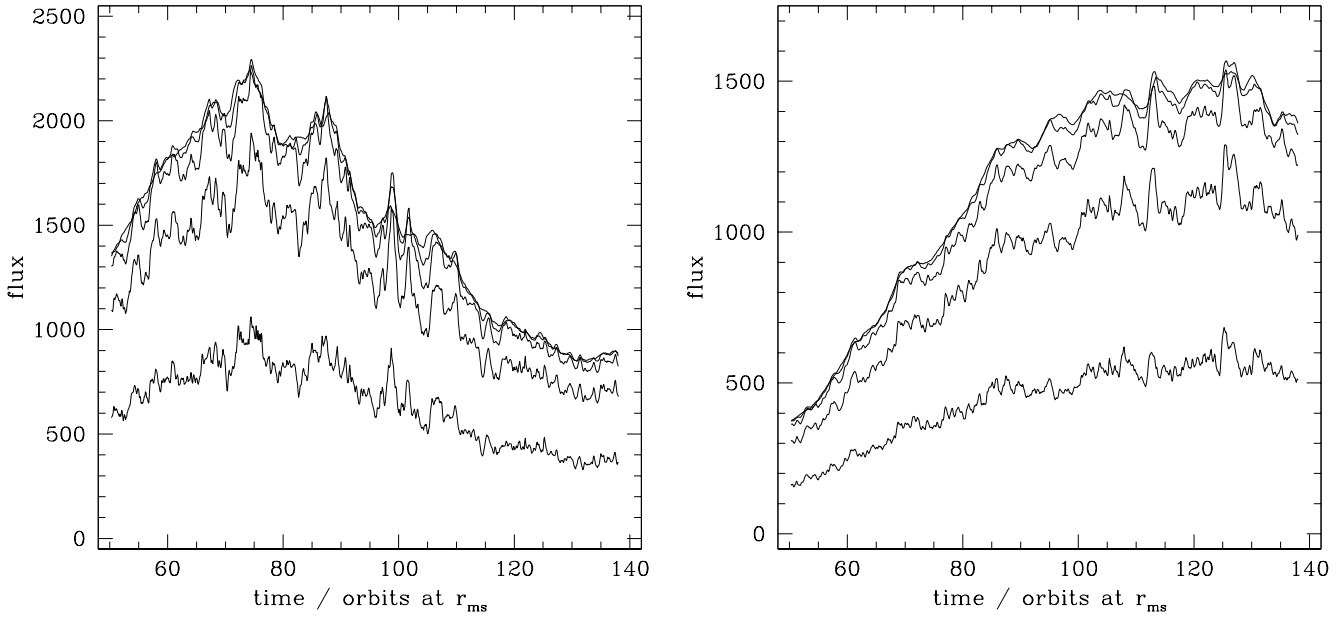


Figure 5. Raw lightcurves showing the integrated flux from the disc as a function of the system inclination. From top downward, $i = 1^\circ, 20^\circ, 40^\circ, 60^\circ, 80^\circ$. The small scale fluctuations increase with increasing system inclination. The hot simulation is displayed in the left panel, whereas the right panel displays the cold simulation.

statistical properties are computed directly from the MHD simulation. Using this normalized dissipation map (which we shall refer to as a ‘NT-normalization’), one can construct the observed emission map and a lightcurve in exactly the manner discussed above.

4.2 The temporal power spectrum

For a given lightcurve, we compute the temporal power spectrum $G(f)$, where f is the frequency, via a straightforward Fourier transform together with the ‘Leahy normalization’,

$$G(f) = \frac{2|\sum_i \mathcal{F}(t_i) \exp(2\pi j f t_i)|^2}{\sum_i \mathcal{F}(t_i)}. \quad (19)$$

We truncate the resulting power spectra at the high-frequency end at the Nyquist frequency (i.e., half of the sampling frequency of the lightcurve) to account for the finite sampling time. In addition, frequencies are rescaled such that the orbital frequency at the radius of marginal stability is unity.

Figure 6 shows power spectra computed using emission that originates from several narrow annuli in the inner disc of the hot simulation. The power spectra are described well by broken power laws. Below a break frequency, which is comparable to the local orbital frequency, $G(f)$ is flat or modestly declining ($G(f) \propto f^{-1}$). At higher frequencies, above the break, we obtain a steep spectrum with $G(f) \propto f^{-3.5}$.

Power spectra computed using the integrated disc emission (ie directly from the lightcurves in Figure 5) are shown in Figures 7 and 8 for the cold and hot runs respectively. For the cold run, $G(f)$ calculated from the raw lightcurve is accurately approximated by a power law with an index of -2

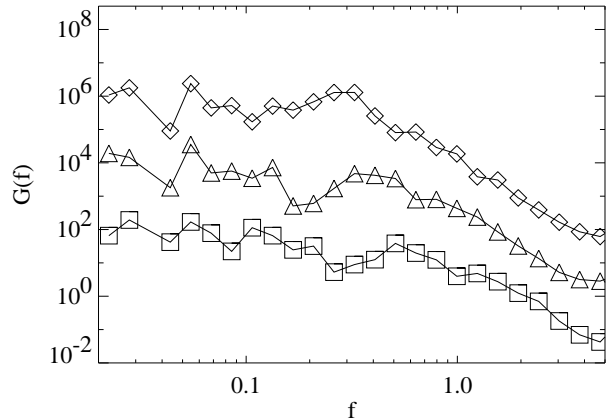


Figure 6. Power spectra of the predicted emission from individual annuli of the hot disc simulation. The system inclination is $i = 50^\circ$. From bottom upward, we show results for annuli defined by $6 < r/r_{\text{ms}} < 7$, $8 < r/r_{\text{ms}} < 9$, and $10 < r/r_{\text{ms}} < 11$. Below a break frequency, which is comparable to the orbital frequency, the power is flat or slowly declining (roughly bracketed by $G(f) = \text{const}$ and $G(f) \propto \nu^{-1}$). At high frequencies, $G(f) \propto \nu^{-3.5}$.

for all frequencies which are accessible using the simulation. There are no significant changes in the slope of $G(f)$ with increasing system inclination. Figure 7 also shows power spectra computed from the NT-normalized lightcurves. Although not identical, these are almost indistinguishable from power spectra calculated using the raw lightcurve. We conclude that the presence of torque at the marginally stable or-

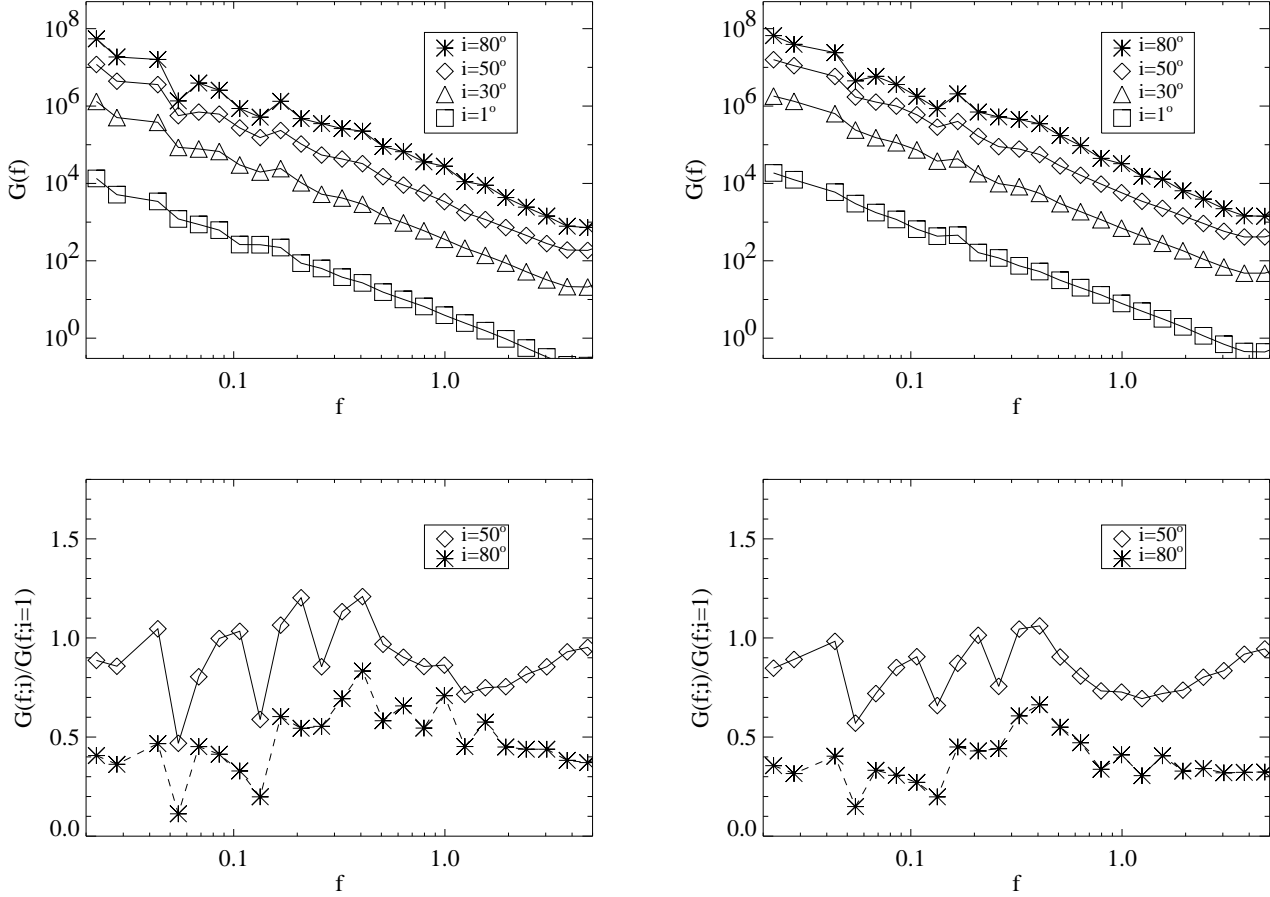


Figure 7. *Upper panels:* Power spectra $G(f)$ for the raw (left) and NT-normalized (right) light curves resulting from the cold simulation. The frequency f has been rescaled such that the orbital frequency at the radius of marginal stability corresponds to $f = 1$. Shown here are the power spectra for $i = 1^\circ$, $i = 30^\circ$ (offset by 10^2), $i = 50^\circ$ (offset by 10^3), and $i = 80^\circ$ (offset by 10^4). *Lower panels:* The ratio $G(f,i)/G(f,i=1)$ for $i = 50^\circ$ and $i = 80^\circ$. This representation helps isolate the effect of inclination on the power spectrum. See text for discussion.

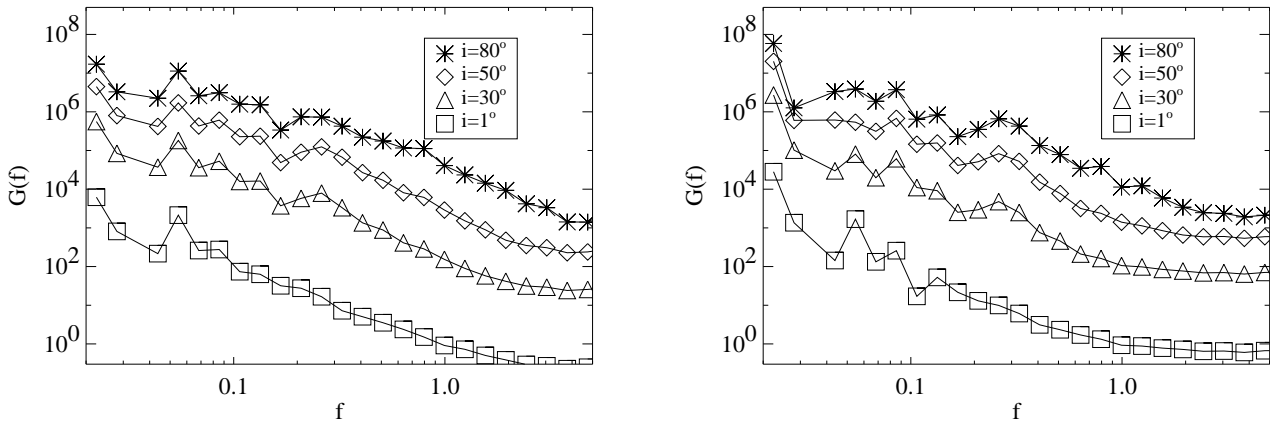


Figure 8. Same as the upper panels in Fig. 7, except here computed for the hot simulation.

bit – at least at the rather modest levels obtained in our calculations – does not significantly affect the predicted power spectrum.

The power spectra shown in Figure 7 appear to be accurately described by single power laws over the range of frequencies accessible using the simulation. Observationally, high frequency QPOs in black hole systems are typically weak features. For example, the broad QPO at 300 Hz reported by Remillard et al. (1999) in GRO J1655-40 had an amplitude of less than 1%. Substantially longer simulations would be needed before we could measure the theoretical power spectrum accurately enough to detect broad QPOs of such small amplitude. We can, however, place limits on the possible existence of stronger QPOs that could arise from the ‘lighthouse’ mechanism discussed by Abramowicz et al. (1991) and Karas (1999). Such QPOs, since they originate from the combination of hotspots with relativistic beaming, should become stronger at higher system inclinations. To investigate this possibility, the lower panels of Figure 7 show the relative power for inclined systems as compared to face-on systems. For $i = 50^\circ$, any QPOs at frequencies comparable to the orbital frequency contribute at most $\approx 20\%$ of the broadband power.

Figure 8 shows the corresponding power spectra extracted from the hot simulation. The results are generally consistent, though the deviations from a power law form for $G(f)$ are larger. At higher inclinations there are some indications of the presence of excess power at a frequency of around 0.2–0.3 times the orbital frequency at r_{ms} . Excess power is also seen in the cold simulation at similar frequencies, though at a lower level. Longer simulations are required to investigate the reality of such weak, broad features.

Since the emission from a particular annulus has a power-spectrum that breaks at the orbital frequency of that annulus, we expect that the disk-integrated power-spectrum should possess a high-frequency break corresponding to the innermost emitting annulus. The overall power-spectra should therefore steepen appreciably above $f \sim 1$. In fact, we do not see such a high-frequency break in Figures 7 and 8. We have investigated the source of this additional high frequency noise in our lightcurves, and find that it originates from emission from the outermost parts of the simulated disc. Our suspicion is that the spatial discretization of the disc into cells – which are physically largest in the outer disc – introduces a low level of high frequency flicker into the lightcurve. This hampers our ability to see high-frequency cutoffs in the disk-integrated power-spectra.

5 IRON LINE VARIABILITY

The broad iron line is one of the best understood observational probes of black hole accretion discs at the present time (e.g., see reviews by Fabian et al. 2000; Reynolds & Nowak 2003). Thus, it is useful to examine the predictions of our simulation for temporal variability of the iron line.

The predicted temporal variability of the iron line obviously depends on how that line is excited. Different authors have computed the iron line response to flares in the inner regions of the flow, using a variety of different geometries and kinematics for the source of exciting photons (Fabian et al. 1989; Stella 1990, Matt & Perola 1992; Reynolds et al.

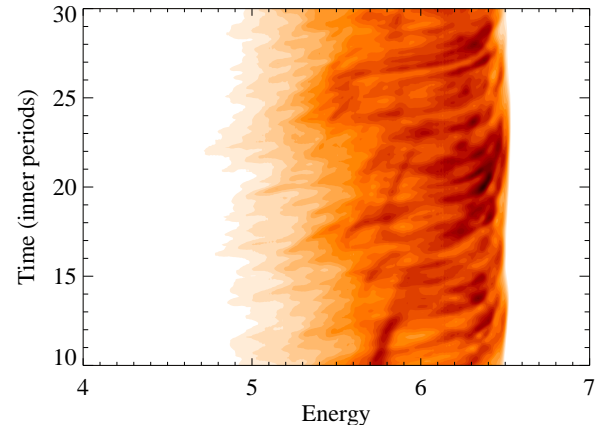


Figure 10. Iron line intensity as a function of energy and time for a 20 orbit segment of our simulation, assuming an inclination of $i = 20^\circ$.

1999; Ruszkowski 2000). In this work, we assume that the local iron line intensity coming from the surface of the disc is proportional to the local continuum intensity (and, hence, is proportional to the local vertically integrated azimuthal magnetic stress). The line intensity at image-plane position (x, y) , time t and energy E is then given by

$$I_{\text{line}}(x, y, t; E) \propto g^4(x, y) F(r, \phi, t_{\text{emit}}) \delta(E - gE_0), \quad (20)$$

where E_0 is the rest-frame energy of the emission line and $F(r, \phi, t)$ is taken to be either the raw or NT-normalized disc flux. Note that the K-correction is not relevant for computing line fluxes and, in this expression, one power of g results from the transformation of the frequency-element. The total simulated observed line is obtained from integrating this expression over the image plane. Figure 9 shows instantaneous iron line profile resulting from the hot simulation for an inclination of $i = 40^\circ$. The skewed and redshifted profile is caused by a combination of the line-of-sight Doppler effect, the transverse Doppler effect (i.e. special relativistic time dilation) and gravitational redshifts (see Fabian et al. 2000 and Reynolds & Nowak 2003 for a detailed discussion of the physics determining these line profiles).

Under the assumptions employed above, the simulated iron line at any particular instant is a weighted redshift map of the turbulent emissivity pattern across the disc. Thus, the temporal and azimuthal variability caused by the MHD turbulence will produce a level of inevitable and irreducible temporal variability in the iron line profile. This can be seen by comparing the instantaneous line profiles in Figure 9. From this figure, it can be seen that the iron line from the hot disc displays dramatic (factor of ~ 2) variability between independent time slices, whereas the line profile from the cold disc is more stable, showing deviations at only the ~ 30 percent level.

The nature of the iron line variability is demonstrated more clearly in Figure 10, which shows the intensity of the simulated iron line emission as a function of energy and time for a representative interval during our simulations, assuming an inclination of $i = 20^\circ$. This is a plausible inclination for many Seyfert-1 nuclei, the systems in which broad iron lines have been best studied to date. One can see a tremen-

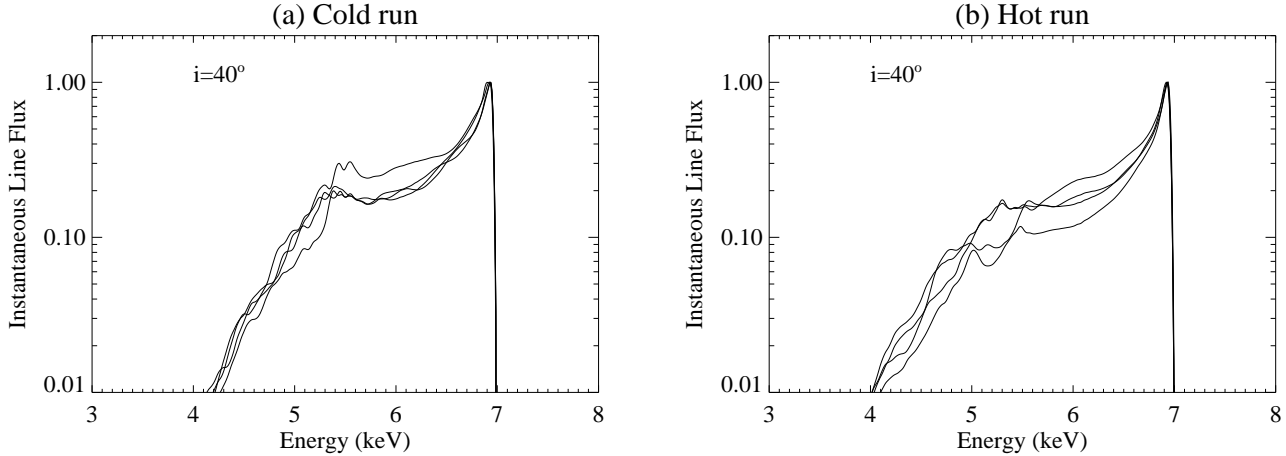


Figure 9. Instantaneous simulated iron line profiles for the cold (left) and hot (right) simulations. Note that the line flux is plotted on a logarithmic vertical scale.

dous degree of structure in the iron line profile as a function of both energy and time. Of particular note are the distinctive arcs that correspond to the orbital motion of especially bright regions within the turbulent flow, visible in Figure 4. These arcs essentially trace out (in the energy-time plane) the paths of test particle with orbits close to the radius of marginally stability. If they could be detected, they would provide a quantitative test of the flow extremely close to the black hole. High temporal resolution is required to observe such features, but the required capabilities should be readily within reach of the planned *Constellation-X* and *XEUS* missions.

In fact, observational evidence for transient non-axisymmetric structure already exists. *Chandra*-HETG observations of the Seyfert-1 galaxy NGC 3516 have found substructure within the well known broad iron line profile of this object (Turner et al. 2002). The substructure has the form of narrow line-line features at rest-frame energies of 5.6 keV, 6.2 keV and 7.1 keV. Plausible explanations exist for the latter two features; the 7.1 keV feature can be readily attributed to the fluorescent K β emission of cold iron, and the 6.2 keV feature might be the ‘Compton shoulder’ of the prominent 6.4 keV K α fluorescent line of cold iron. However, the 5.6 keV feature cannot be attributed to any expected features. Turner et al. suggest that this feature is, in fact, iron K α fluorescence with a rest-frame energy of 6.4 keV from an anomalously bright annulus or spot on the accretion disc surface. The flux contained in the 5.6 keV feature is approximately 5% of that contained in the overall broad iron line.

Is it possible to relate the substructure observed in the NGC 3516 iron line with the turbulence induced substructure seen in our simulations? While large amplitude substructure is present in virtually every *instantaneous* simulated line profile, it is much diminished once the line profiles are averaged over more than a few orbits. The *Chandra*-HETG observation of Turner et al. that yielded the clear detection of the iron line substructure was 8×10^4 s in duration. Assuming a black hole mass of $2.3 \times 10^7 M_\odot$ (estimated using the velocity dispersion from di Nella et al. 1995, in conjunction with the scaling relations of Gebhardt et al.

2000 or Ferrarese & Merritt 2000)³, this corresponds to approximately 20 orbital periods of the accretion disc at the radius of marginal stability. Thus, to compare our simulations to these data, we averaged our simulated line profiles over 20 orbits of the inner disc. We assumed a disc inclination of $i = 40^\circ$ (Wu & Han 2001). Given the useful length of our simulation, five independent 20-orbit line profiles could be formed. We found that 4 out of 5 of these profiles possessed no strong deviations from the average. In one profile, however, there was a slight excess centered at an energy of 5.5 keV, possessing 2–3% of the total flux. Therefore, while the true interpretation of the *Chandra* data for NGC 3516 remains unclear, turbulence-induced substructure is a viable possibility even when one considers that the disc has likely undergone several orbits during the observation.

6 SUMMARY

In this paper, we have explored the predicted variability of accretion discs around Schwarzschild black holes. The temporal and spatial fluctuations in the magnetic stress which drives accretion have been calculated using three-dimensional global simulations in a pseudo-Newtonian potential, which ought to provide a reasonable first approximation to the disc dynamics outside the marginally stable orbit. By making the further critical assumption that the radiation from the disc follows the local stress, we have calculated the predicted emission that would be seen by an observer using a fully relativistic ray-tracing code that accounts for the relativistic effects of beaming, gravitational redshift, and light bending.

Our results for the temporal power spectrum of the predicted emission are consistent with those of previous authors (Kawaguchi et al. 2000; Hawley & Krolik 2001, 2002). Fluctuations in the magnetic stress, when integrated across the disc, produce a high frequency power spectrum described

³ Independent estimates of the black hole mass are comparable. For example, Onken et al. (2003) estimate $M_{BH} = 1.7 \times 10^7 M_\odot$ from reverberation mapping.

by a power law with slope f^{-2} . To a first approximation, observers viewing the system at a wide range of inclinations – from face-on to almost edge-on – are predicted to derive similar power spectra. In more detail, high inclinations are found to boost the relative power at frequencies a factor of a few below the orbital frequency at the marginally stable orbit. There is little change in the predicted power spectra due to the presence or absence of modest levels of magnetic stress at the marginally stable orbit. No strong QPOs are seen in the simulations, though weak features could be present and would not be clearly observed given the limited statistics available from $\approx 10^2$ orbit simulations.

The broad iron line provides an alternate probe of conditions in the inner disc, and has the advantage of retaining velocity information. We have used the simulations to quantify the predicted iron line variability within a model in which the local iron line emissivity tracks the locally generated continuum emission. This model represents the opposite extreme from reverberation models, in which the source of line exciting flux is often assumed to be widely spatially separated from the disc. We find that order unity fluctuations in the line flux at fixed energy occur for discs with $h/r \sim 0.1$, with the fluctuation amplitude increasing rapidly with increasing disc thickness. Averaging over *at least* several orbits at the radii of interest is needed before meaningful averages can be extracted (see also Papaloizou & Nelson 2003; Winters, Balbus & Hawley 2003). Observationally, this implies that long integrations, extending over tens of orbital timescales, are required in order to reduce the fluctuation amplitude to percent levels and thereby recover the mean line profile.

ACKNOWLEDGEMENTS

We thank Cole Miller, Eve Ostriker, Daniel Proga and Mateusz Ruszkowski for extensive discussions, and Pete Ruprecht for assisting with computational support. We thank the referee for providing an extremely prompt report on the paper. CSR acknowledges support from the National Science Foundation under grant AST0205990.

REFERENCES

Abramowicz M.A., Bao G., Lanza A., Zhang X.-H., 1991, A&A, 245, 454

Afshordi N., Paczynski B., 2003, ApJ, submitted, astro-ph/0202409

Agol E., Krolik J.H., 2000, ApJ, 528, 161

Arlt R., Rudiger G., 2001, A&A, 374, 1035

Armitage P.J., 1998, ApJ, 501, L189

Armitage P.J., Reynolds C.S., Chiang J., 2001, ApJ, 548, 868

Balbus S.A., Hawley J.F., 1991, ApJ, 376, 214

Balbus S.A., Hawley J.F., 1998, Rev. Mod. Phys., 70, 1

Balucinska-Church M., Church M.J., 2000, MNRAS, 312, L55

Brandenburg A., Nordlund A., Stein R.F., Torkelsson U., 1995, ApJ, 446, 741

di Nella, H.; Garcia, A. M.; Garnier, R.; Paturel, G., 1995, A&AS, 113, 151

Evans C.R., Hawley J.F., 1988, ApJ, 332, 659

Fabian A.C., Rees M.J., Stella L., White N.E., 1989, MNRAS, 238, 729

Fabian A.C., Iwasawa K., Reynolds C.S., Young A.J., 2000, PASP, 112, 1145

Ferrarese L., Merritt D., 2000, ApJ, 539, L9

Gammie C.F., 1999, ApJ, 522, L57

Gebhardt K. et al., 2000, ApJ, 539, L13

Hawley J.F., 2000, ApJ, 528, 462

Hawley J.F., 2001, ApJ, 554, 534

Hawley J.F., Balbus S.A., Stone J.M., 2001, ApJ, 554, L49

Hawley J.F., Gammie C.F., Balbus S.A., 1995, ApJ, 440, 742

Hawley J.F., Krolik J.H., 2001, ApJ, 548, 348

Hawley J.F., Krolik J.H., 2002, ApJ, 566, 164

Hubeny I., Hubeny V., 1998, ApJ, 505, 558

Igumenshchev I.V., Narayan R., 2002, ApJ, 566, 137

Igumenshchev I.V., Narayan R., Abramowicz M.A., 2003, ApJ, submitted, astro-ph/0301402

Iwasawa K., 1996, MNRAS, 282, 1038

Karas V., 1999, PASJ, 51, 317

Kawaguchi T., Mineshige S., Machida M., Matsumoto R., Shibata K., 2000, PASJ, 52, L1

Krolik J.H., 1999, ApJ, 515, L73

Lee J.C., Iwasawa K., Houck J.C., Fabian A.C., Marshall H.L., Canizares C.R., 2002, ApJ, 570, L47

Lubow S.H., Papaloizou J.C.B., Pringle J.E., 1994, MNRAS, 267, 235

Machida M., Matsumoto R., 2003, ApJ, in press, astro-ph/0211240

Machida M., Matsumoto R., Mineshige S., 2001, PASJ, 53, L1

Matt G., Perola G.C., 1992, MNRAS, 259, 433

Miller J.M. et al., 2002, ApJ, 578, 348

Miller K.A., Stone J.M., 2000, ApJ, 534, 398

Nandra K., George I.M., Mushotzky R.F., Turner T.J., Yaqoob, T., 1997, ApJ, 477, 602

Novikov I.D., Thorne K.S., 1973, in Black Holes, eds. C. DeWitt & B.S. DeWitte (New York: Gordon and Breach), p. 344

Onken C.A., Peterson B.M., Dietrich M., Robinson A., Salamanca I.M., 2003, ApJ, in press, astro-ph/0212115

Paczynski B., Wiita P.J., 1980, A&A, 88, 23

Page D.N., Thorne K.S., 1974, ApJ, 191, 499

Papaloizou J.C.B., Nelson R.P., 2003, MNRAS, in press, astro-ph/0211493

Rauch K.P., Blandford R.D., 1994, ApJ, 421, 46

Remillard R.A., Morgan E.H., McClintock J.E., Bailyn C.D., Orosz J.A., 1999, ApJ, 522, 397

Reynolds C.S., Armitage P.J., 2001, ApJ, 561, L81

Reynolds C.S., Nowak M.A., 2003, Physics Reports, in press, astro-ph/0212065

Reynolds C.S., Young A.J., Begelman M.C., Fabian A.C., 1999, ApJ, 514, 164

Ruszkowski M., 2000, MNRAS, 315, 1

Steinacker A., Papaloizou J.C.B., 2002, ApJ, 571, 413

Stella L., 1990, Nature, 344, 747

Stone J.M., Norman M.L., 1992a, ApJS, 80, 753

Stone J.M., Norman M.L., 1992b, ApJS, 80, 791

Strohmayer T.E., 2001, ApJ, 554, L169

Tanaka Y. et al., 1995, Nature, 375, 659

Turner T.J. et al., 2002, ApJ, 574, L123

van der Klis M., 2000, ARA&A, 38, 717

Wilms J., Reynolds C.S., Begelman M.C., Reeves J., Molendi S., Staubert R., Kendziorra E., 2001, MNRAS, 328, L27

Winters W.F., Balbus S.A., Hawley J.F., 2003, MNRAS, in press, astro-ph/0301498

Wu X.-B., Han J.L., 2001, ApJ, 561, L59